# Climate Data Record (CDR) Program

## Climate Algorithm Theoretical Basis Document (C-ATBD)

## AVHRR Land Bundle - Surface Reflectance and Normalized Difference Vegetation Index

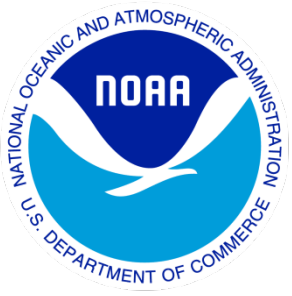


CDR Program Document Number: CDRP-ATBD-0459
Configuration Item Number: 01B-20a & 01B-20b
Revision 2 / August 22, 2018

# REVISION HISTORY

| Rev. | Author | DSR No. | Description | Date |
|---|---|---|---|---|
| 1 | Eric Vermote, NASA and Martin Claverie, NASA | DSR-552 | Initial Submission to CDR Program | 11/18/2013 |
| 2 | Eric Vermote | DSR-1274 | Version 5 corrects for known errors in time, latitude, and longitude variables as well as global and variable attribute definitions. Scientific improvements include updating to higher resolution ancillary data and more accurate approaches for BRDF correction, calibration, compositing, and QA . | 8/22/2018 |
| | | | | |
| | | | | |
| | | | | |
| | | | | |
| | | | | |
| | | | | |
| | | | | |
| | | | | |

# TABLE of CONTENTS

## LIST of FIGURES

# LIST of TABLES

# 1. Introduction

## 1.1 Purpose

The purpose of this document is to describe the algorithm submitted to the National Centers for Environmental Information (NCEI) by Dr. Eric Vermote, NASA/GSFC, Terrestrial Information Systems Branch, Code 619, that will be used to create the AVHRR Surface Reflectance and Normalized Difference Vegetation Index Climate Data Record (CDR), using Advanced Very High Resolution Radiometer (AVHRR) sensors onboard the NOAA 7, 9, 11, 14, 16, 17, and 18 platforms. The actual algorithm is defined by the computer program (code) that accompanies this document, and thus the intent here is to provide a guide to understanding that algorithm, from both a scientific perspective and in order to assist a software engineer or end-user performing an evaluation of the code.

## 1.2 Definitions

Following is a summary of the symbols used to define the algorithm.

Spectral and directional parameters:

$\theta_s$ = *sun zenith angle.* (1)

$\theta_v$ = *view zenith angle.* (2)

$\mu_s$ =*cos(sun zenith angle) .* (3)

$\mu_v$ = =*cos(view zenith angle) .* (4)

$\xi$ *is the phase angle.* (5)

$\Phi$ = *view-sun relative azimuth.* (6)

$\rho$ = *reflectance.* (7)

$\tau$ = *aerosol optical thickness.* (8)

$\omega_{os}^{\lambda}$ = *spectral single scattering albedo.* (9)

*L = radiance.* (10)

*Fo = solar radiance.* (11)

$F_1$ = *volume scattering kernel.* (12)

$F_2$ = *geometric kernel.* (13)

*k0, k1, k2 = BRDF kernel coefficient.* (14)

*p = pressure.* (15)

*T = transmittance.* *(16)*

$T^{\uparrow}$ *= upward transmittance.* *(17)*

$T^{\downarrow}$ *= downward transmittance.* *(18)*

$T_g$ *=gaseous transmission for gases.* *(19)*

$t_d$ *= diffuse transmittance .* *(20)*

*S = reflectance of the atmosphere for isotropic light entering the base of the atmosphere.* *(21)*

*Ux = Concentration in x component.* *(22)*

*V, R = BRDF coefficients.* *(23)*

## 1.3 Referencing this Document

This document should be referenced as follows:

AVHRR Surface Reflectance and Normalized Difference Vegetation Index - Climate Algorithm Theoretical Basis Document, NOAA Climate Data Record Program CDRP-ATBD-0459 Rev. 2 (2018). Available at http://www.ncdc.noaa.gov/cdr/operationalcdrs.html

## 1.4 Document Maintenance

Periodic updates to the algorithm and dataset are possible to occur. This could be (for example) when improvements to the algorithm are developed. Any update will be given a new version number, and an updated version of the C-ATBD will be generated.

# 2. Observing Systems Overview

## 2.1 Products Generated

The objective of this algorithm is to retrieve the Bidirectional reflectance distribution function (BRDF)-corrected Surface Reflectance and the associated Normalized Difference Vegetation Index (NDVI) from AVHRR sensors. Additional products are provided such as cloud, cloud-shadows snow masks. The final products are mapped into daily 0.05°x0.05° grid, corresponding to a 3600x7200 array over the globe.

## 2.2 Instrument Characteristics

Surface Reflectance products will be generated for each cloud-free pixel (0.05°x0.05°) observed by the AVHRR imager channel 1-3. Channels 3-5 are used to retrieve atmospheric conditions, (e.g., water vapor) cloud and snow masks. Timeline of the NOAA platform numbers is presented in Figure 1.

**Table 1: Example of AVHRR channels and the channels selected for aerosol retrieval. Channel 3a is only available for the AVHRR instrument on NOAA-16, -17, -18.**

| Channel number | Wavelength (μm) |
|---|---|
| 1 | 0.63 |
| 2 | 0.83 |
| 3a | 1.61 |
| 3b | 3.75 |
| 4 | 11.0 |
| 5 | 12.0 |

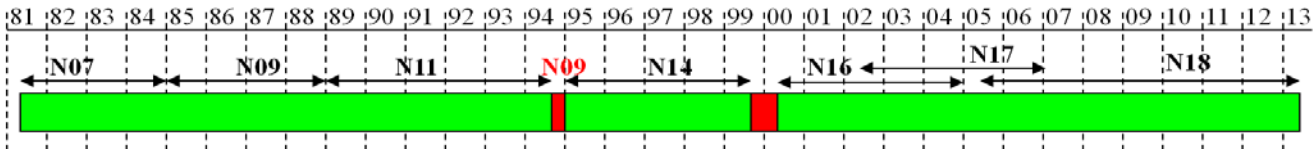


**Figure 1: Timeline of the NOAA platform numbers.**

# 3. Algorithm Description

## 3.1 Algorithm Overview

This is the complete description of the algorithm at the current level of maturity (which will be updated with each revision). The algorithm includes retrieval of land Surface Reflectance for Channel 1-3 of AVHRR, the associated NDVI, and corresponding cloud, cloud/shadow and snow masks.

## 3.2 Processing Outline

The processing outline of the AVHRR SR data processing is summarized in the Data Flow Diagram of Figure 2.

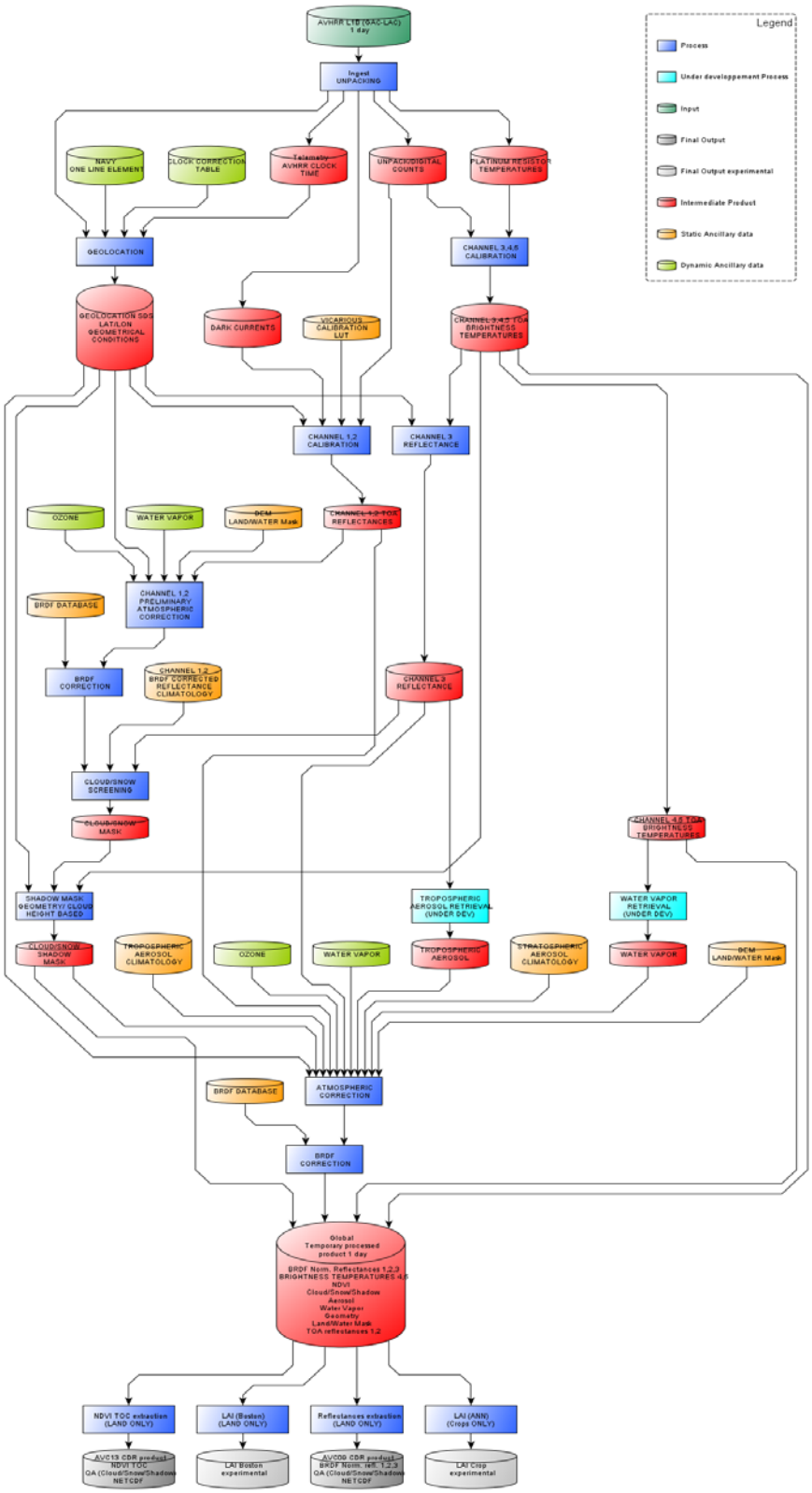


**Figure 2: Global processing outlines Data Flow Diagram of this algorithm.**

The following diagrams in Figures 3-8 refer to the same flowchart of Figure 2, except that processes were divided in 6 flowcharts.

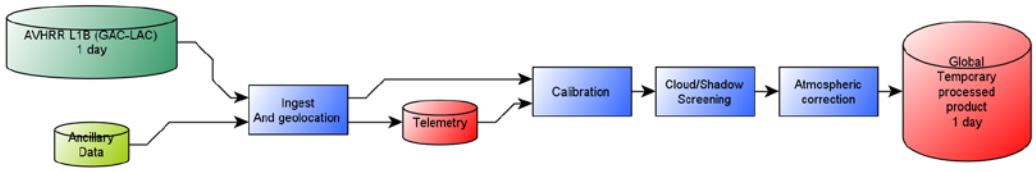


**Figure 3: Processing outline flowchart of this algorithm: Step 1**

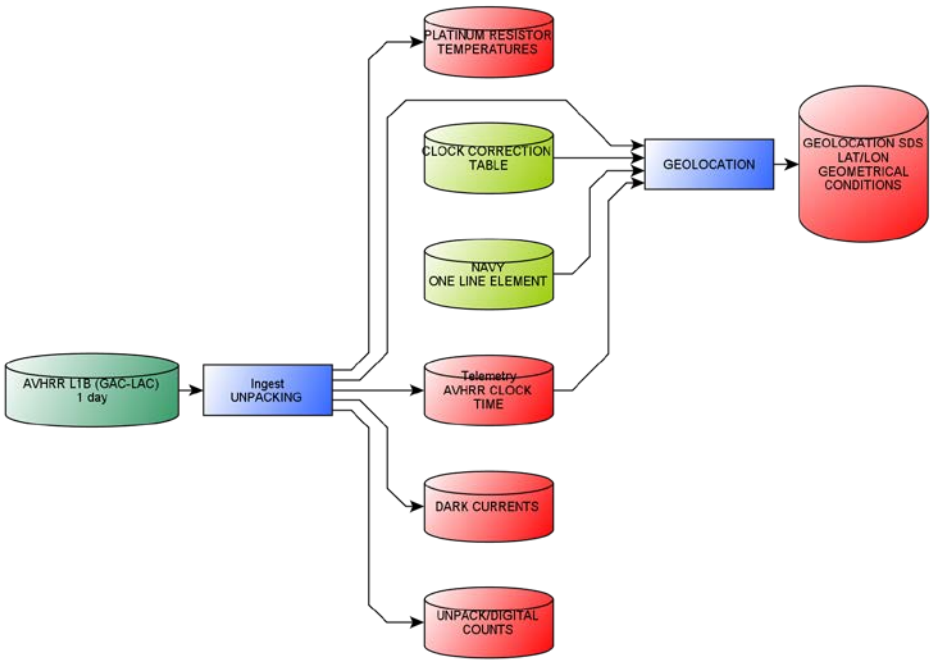


**Figure 4: Processing outline flowchart of this algorithm: Step 2**

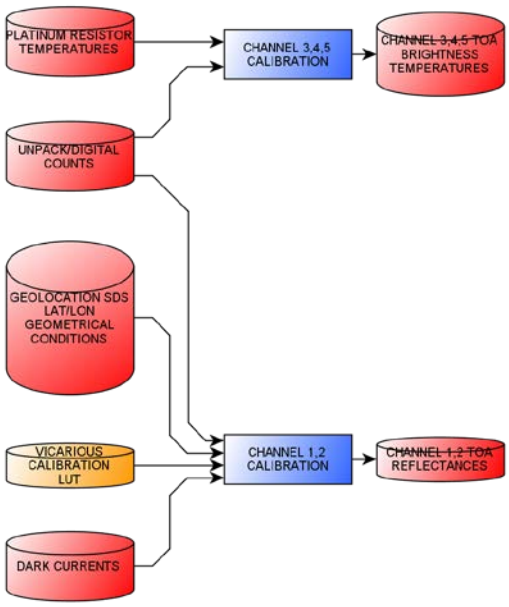


**Figure 5: Processing outline flowchart of this algorithm: Step 3**

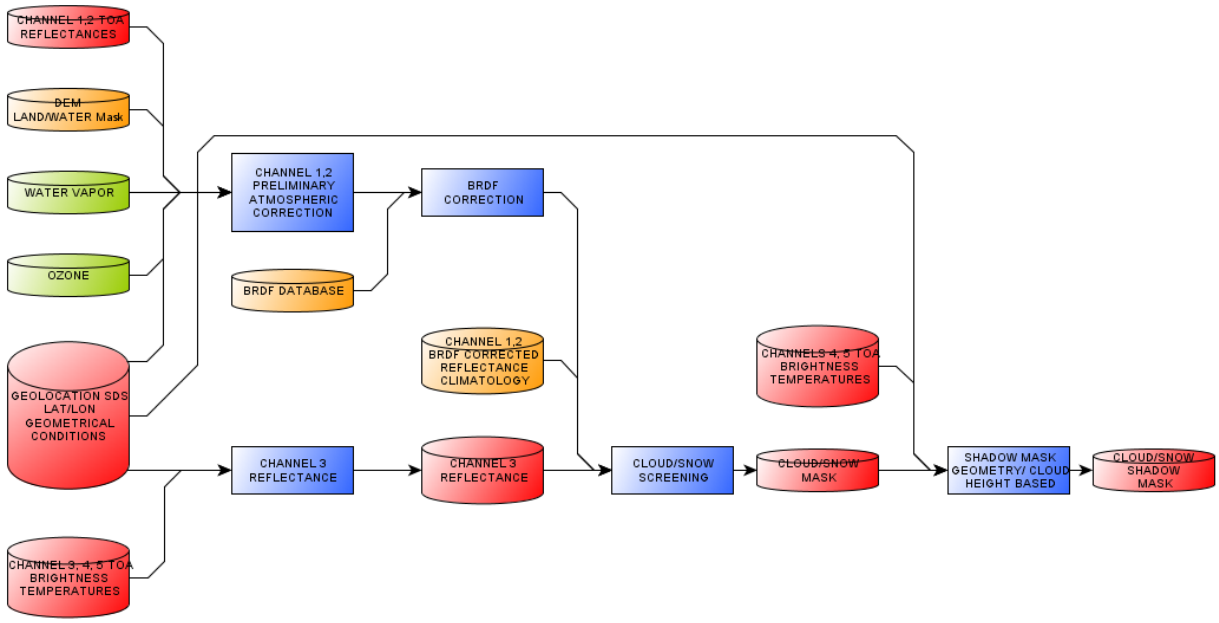


**Figure 6: Processing outline flowchart of this algorithm: Step 4**

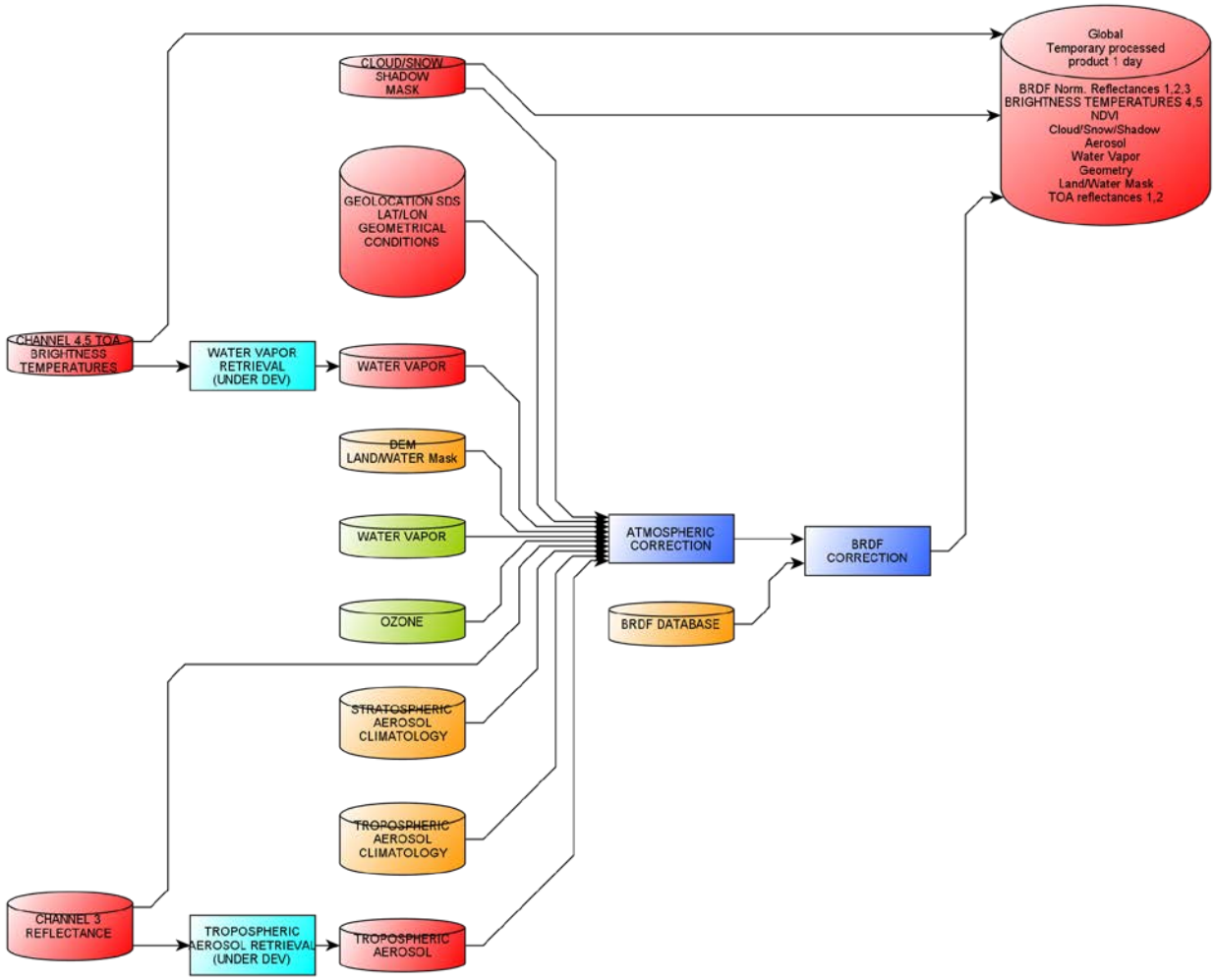


**Figure 7: Processing outline flowchart of this algorithm: Step 5**

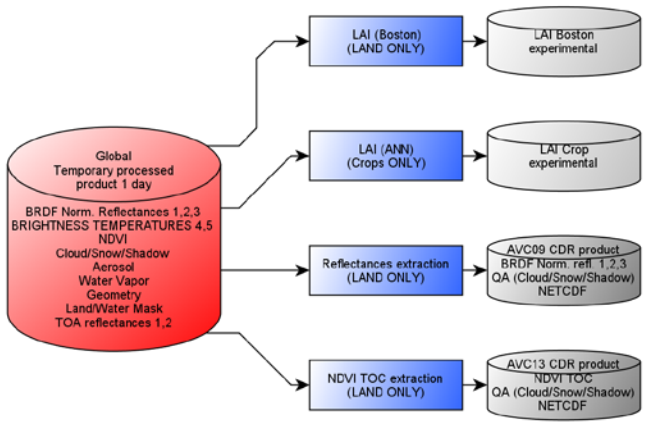


**Figure 8: Processing outline flowchart of this algorithm: Step 6**

# 3.3 Algorithm Input

## 3.3.1 Primary Sensor Data

Primary Sensor Data are calibrated and geolocated AVHRR Global Area Coverage (GAC) 'Level 1B' reflectance at 2 channels and brightness temperature at 3 channels from AVHRR sensor, geolocation information, and sensor data quality flags. Data are described in Table 2.

**Table 2: Primary AVHRR sensor GAC input data**

| Name | Type | Description | Dimension (spatial resolution) |
|---|---|---|---|
| TOA reflectances (Channels 1-2) | Input | Calibrated AVHRR TOA reflectance | Scan line (4km x 4km) |
| TOA Brightness Temperature (Channels 3-5) | Input | Calibrated AVHRR TOA Brightness Temperature | Scan line (4km x 4km) |
| Latitude | Input | Pixel latitude | Scan line (4km x 4km) |
| Longitude | Input | Pixel longitude | Scan line (4km x 4km) |
| Solar geometry | Input | Solar zenith and azimuth angles | Scan line (4km x 4km) |
| View geometry | Input | View zenith and azimuth angles | Scan line (4km x 4km) |
| QC flags | Input | Quality control flags with level 1B data | Scan line (4km x 4km) |

## 3.3.2 Ancillary Data

The Surface reflectance algorithm requires ancillary data listed in Table 3.

**Table 3: Ancillary Data**

| Name | Type | Source | Spatial resolution |
|---|---|---|---|
| NAVY ONE LINE ELEMENT | Input | Navy | - |
| CLOCK CORRECTION TABLE | Input | SCD group | - |
| VICARIOUS CALIBRATION LUT | Input | Internal | - |
| OZONE | Input | GDAS | 0.5° |
| WATER VAPOR | Input | GDAS/MODIS | 0.5°/0.05° |
| STRATOSPHERIC AEROSOL CLIMATOLOGY | Input | Internal | - |
| TROPOSPHERIC AEROSOL CLIMATOLOGY | Input | Internal | - |
| DEM | Input | USGS | 0.05° |
| LAND/WATER Mask | Input | MODIS | 0.05° |
| BRDF DATABASE | Input | MODIS | 0.05° |
| CHANNEL 1,2 BRDF CORRECTED REFLECTANCE CLIMATOLOGY | Input | MODIS | 0.05° |

### 3.3.3 Derived Data

<Not Applicable>

### 3.3.4 Forward Models

<Not Applicable>

## 3.4 Theoretical Description

In this section we describe the algorithms which will make the atmospheric corrections and the BRDF correction.

### 3.4.1 Physical and Mathematical Description

#### 3.4.1.1 Atmospheric correction

The radiance in the solar spectrum which reaches the AVHRR instrument at the top of the atmosphere valid for Lambertian surface reflectance, can be described as

$$L_{TOA}(\mu_s,\mu_v,\phi) = L_0(\mu_s,\mu_v,\phi) + \frac{T(\mu_s)T(\mu_v)F_0\mu_s\rho_s(\mu_s,\mu_v,\phi)}{\pi[1-\rho_s(\mu_s,\mu_v,\phi)S]} \quad (24)$$

where $L_{TOA}$ is the radiance received by the satellite at the top of the atmosphere, $L_o$ is the path radiance, $T(\mu_s)$ is the total transmittance from the top of the atmosphere to the ground along the path of the incoming solar beam, $T(\mu_v)$ is the total transmittance from the ground to the top of the atmosphere in the view direction of the satellite, $F_o$ is the solar radiance at the top of the atmosphere, $\rho_s(\mu_s,\mu_v,\varphi)$ is the surface reflectance with no atmosphere above it, S is the reflectance of the atmosphere for isotropic light entering the base of the atmosphere, $\mu_s$ is the cosine of the solar zenith angle, $\mu_v$ is the cosine of the view angle and $\varphi$ is the azimuthal difference between the two zenith angles. The radiances in Eq. 24 can be normalized by the incident solar radiance, $F_o\,\mu_s/\pi$, which results in the following equation:

$$\rho_{TOA}(\mu_s,\mu_v,\phi) = \rho_0(\mu_s,\mu_v,\phi) + \frac{T(\mu_s)T(\mu_v)\rho_s(\mu_s,\mu_v,\phi)}{[1-\rho_s(\mu_s,\mu_v,\phi)S]} \quad (25)$$

where $\rho_{TOA}$ is the reflectance at the top of the atmosphere and $\rho_0$ is path radiance in reflectance units. T is divided into direct and diffusive parts as

$$T(\mu) = e^{-\tau/\mu} + t_d(\mu) \quad (26)$$

for $\mu = \mu_s, \mu_v$, where $\tau$ is the total optical thickness and $t_d$ the diffuse transmittance.

### 3.4.1.2 Rayleigh Scattering

Scattering by the gaseous constituents of the air is a well-defined problem depending only on the wavelength of the radiation, air pressure and temperature profiles. In the radiative transfer code used here, pressure and temperature profiles are given by McClatchey et al. (1971) where different profiles are described for various climatic regions and seasons. Surface altitude information for each pixel will be available through a digital elevation model at the resolution of 5 minutes (ETOPO5, NOAA, 1988), which is roughly 8 km by 8 km. The algorithm assumes a surface elevation of 0 km for use by the radiative transfer code and adjust the Rayleigh outputs in the look-up table for variations in elevation and Global Assimilation Model output if available (Fraser et al, 1989; Fraser et al., 1992).

### 3.4.1.3 Stratospheric aerosol

The stratosphere may at times have a significant optical thickness due to volcanic eruptions. These aerosol layers may cover a large portion of the globe and persist on the time scales of months to years. This phenomenon can seriously compromise vegetation monitoring. An example is the Pinatubo eruption of 1991 (Vermote et al, 1994). The stratospheric aerosol optical thickness may be determined from MODIS algorithms using the 1.38 μm channel (Kaufman and Tanré, 1998) or it may be provided from other sources e.g. Stratospheric Aerosol and Gas Experiment (SAGE) instrument (McCormick and

Vega, 1992). The stratospheric phase function will be obtained from King et al. (1984) who used El Chichon data to determine the properties of volcanic aerosol in the stratosphere. The single scattering albedo, $\omega_{os}^{\lambda}$ for the stratospheric aerosol will be computed from the refractive indices tabulated by Lenoble (1993).

Not only must $\tau$ be determined for the column, but it must be decoupled into stratospheric and tropospheric components. During an important volcanic eruption (e.g. Mt Pinatubo, Figure 9) interpreting the aerosol as being located entirely in the troposphere will result in errors on the order of up to several hundredths in reflectance units.

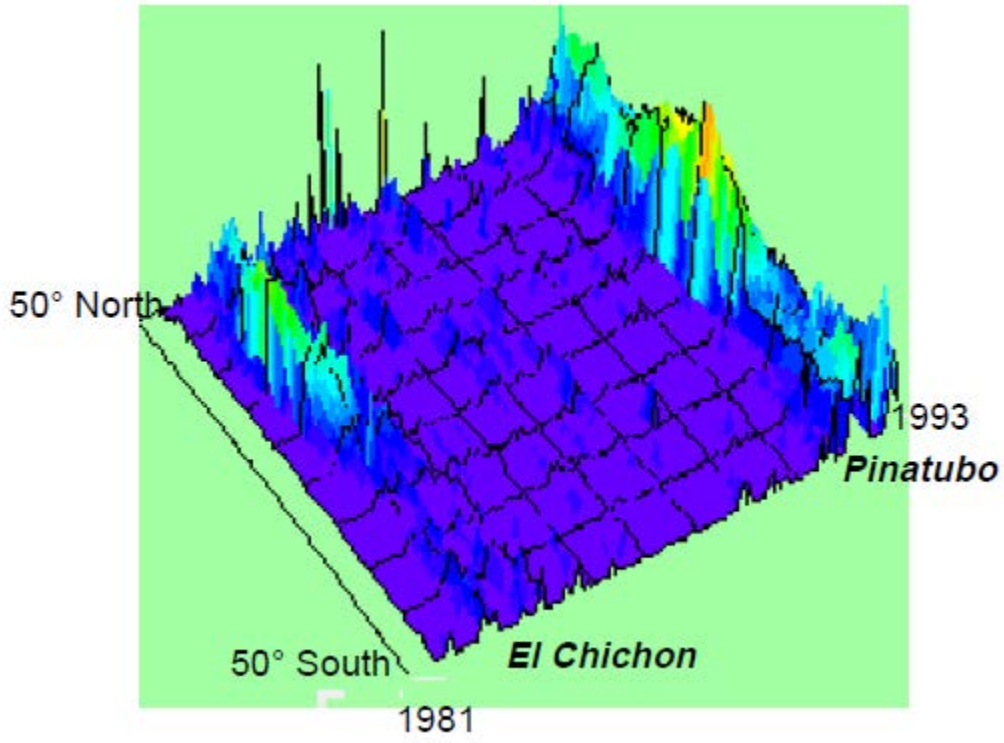


**Figure 9: Monthly average of the stratospheric aerosol optical depth deduced from AVHRR data showing major eruptions of El Chichon and Pinatubo.**

### 3.4.1.4 Gaseous Absorption

To account for gaseous absorption, the reflectance at the top of the atmosphere, $\rho_{TOA}(\mu_s,\mu_v,\varphi)$, is modified as:

$$\rho_{TOA}(\theta_s,\theta_v,\phi_s-\phi_v) = Tg(O_3,O_2,CO_2,M)\begin{bmatrix}\rho_R+(\rho_0-\rho_R)Tg^{H_2O}\left(M,\frac{U_{H_2O}}{2}\right)\\ +T^{\downarrow}(\theta_s)T^{\uparrow}(\theta_v)\frac{\rho_s}{1-S\rho_s}Tg^{H_2O}\left(M,U_{H_2O}\right)\end{bmatrix} \quad (27)$$

Where $\rho_R$ is the molecular intrinsic reflectance, $T^{\downarrow}$ and $T^{\uparrow}$ are the downward and upward transmittance, respectively. M is the air mass, given by:

$$M = \frac{1}{\mu_s} + \frac{1}{\mu_v} \quad (28)$$

$Tg(O_3,O_2,CO_2,M)$ is the gaseous transmission of $O_3$, $O_2$ and $CO_2$ and $Tg^{H2O}$ is the water vapor transmission. The 6S radiative transfer model (Vermote et al., 1997) is used to calculate the gaseous transmission for each gas in each land band for a range of total amount of gas and a range of view angles.

$$T_g(O_3, M) = \exp\left(-aMU_{O_3}\right) \quad (29)$$

where $U_{O3}$ is the total amount ozone in units of cm/atm and a is a coefficient which depends on the response of the given spectral band. Details can be found in Tanré et al. (1990).

The formula adopted for oxygen and carbon dioxide is:

$$Tg(M, \frac{p}{p_0}) = 1 + a_{0g} M_{0g}^{b} \left[ \frac{1}{1 + c_{0g} \frac{p}{p_0} d_{0g} (\frac{p}{p_0})^2} - 1 \right] \quad (30)$$

p is the pressure at the altitude z and $p_0$ is the pressure at sea level. Oxygen and carbon dioxide are taken to be constant and are given in units of parts per billion, their amount is directly provided by the altitude. The parameters a, b, c and d are adjusted for the AVHRR spectral responses.

The total precipitable water UH2O [g/cm2] is a MODIS product (Gao and Kaufman, 1993). It is assumed that the path radiance, ρo, is generated above the middle of the boundary layer. Thus the additional attenuation is made by half the precipitable water. The formula adopted for the water vapor transmission is:

$$Tg(H_2O, M) = exp\left[-exp(a_{H_2O} + b_{H_2O} ln(MU_{H_2O}) + c_{H_2O}\left[ln^2(MU_{H_2O})\right])\right] \quad (31)$$

with a', b', and c' adjusted for the AVHRR spectral responses.

### 3.4.1.5 BRDF correction

The analysis of Parasol multidirectional data has shown that, among analytical BRDF models, the Ross–Li–Maignan model provides the best fit to the measurements (Breon et al. 2002). This model computes the reflectance as the sum of three terms:

$$\rho(\theta_s, \theta_v, \phi) = k_0 + k_1 F_1(\theta_s, \theta_v, \phi) + k_2 F_2(\theta_s, \theta_v, \phi)$$
$$= k_0 \left[1 + \frac{k_1}{k_0} F_1(\theta_s, \theta_v, \phi) + \frac{k_2}{k_0} F_2(\theta_s, \theta_v, \phi)\right] \quad (32)$$

where $F_1$ is the volume scattering kernel, based on the Ross-thick function, but corrected for the Hot-Spot process, and $F_2$ is the geometric kernel, based on the Li-sparse reciprocal function. $F_1$ and $F_2$ are fixed functions of the observation geometry, but $k_0$, $k_1$, and $k_2$ are free parameters. In the following, we will use V as $k_1/k_0$ and R for $k_2/k_0$. The $F_1$ and $F_2$ functions are given in (14) and (15).

$$F_1(\theta_s, \theta_v, \varphi) = \frac{m}{\pi}(t - \sin t \cos t - \pi) + \frac{1 + \cos\xi}{2\cos\theta_s \cos\theta_v}$$

$$\cos t = \frac{2}{m}\sqrt{\Delta^2 + (\tan\theta_s \tan\theta_v \sin\varphi)^2}$$

$$m = \frac{1}{\cos\theta_s} + \frac{1}{\cos\theta_v} \quad (33)$$

$$F_2(\theta_s, \theta_v, \varphi) = \frac{4}{3\pi}\frac{1}{\cos\theta_s + \cos\theta_v}\left[\left(\frac{\pi}{2} - \xi\right)\cos\xi + \sin\xi\right]$$
$$\times \left(1 + \left(1 + \frac{\xi}{\xi_0}\right)^{-1}\right) - \frac{1}{3} \quad (34)$$

where ξ is the scattering angle and $\xi_0$ is a characteristic angle that can be related to the ratio of scattering element size and the canopy vertical density ($\xi_0$ =1.5°).

A correction of the directional effect is derived after transforming the measurement coordinates to standard observation geometry. In the following, the standard observation geometry is for the Sun at 45° from zenith, and the observation at nadir. The normalized reflectance is therefore computed as

$$\rho^N(45, 0, 0) = \rho(\theta_s, \theta_v, \phi)$$
$$\times \frac{1 + VF_1(45, 0, 0) + RF_2(45, 0, 0)}{1 + VF_1(\theta_s, \theta_v, \phi) + RF_2(\theta_s, \theta_v, \phi)} \quad (35)$$

BRDF correction is based on pre-computed coefficients of V and R relationship with NDVI (Vermote et al. 2009).

V = V_slope * NDVI + V_intercep

R = R_slope * NDVI + R_intercep *(36)*

The 4 coefficients (V_slope, V_intercep, R_slope, R_intercep) were retrieved using the 2000-2011 MODIS archives following the approach presented in Vermote et al. 2009. Figure 10 illustrate V and R global maps derived from MODIS 2000-2004.

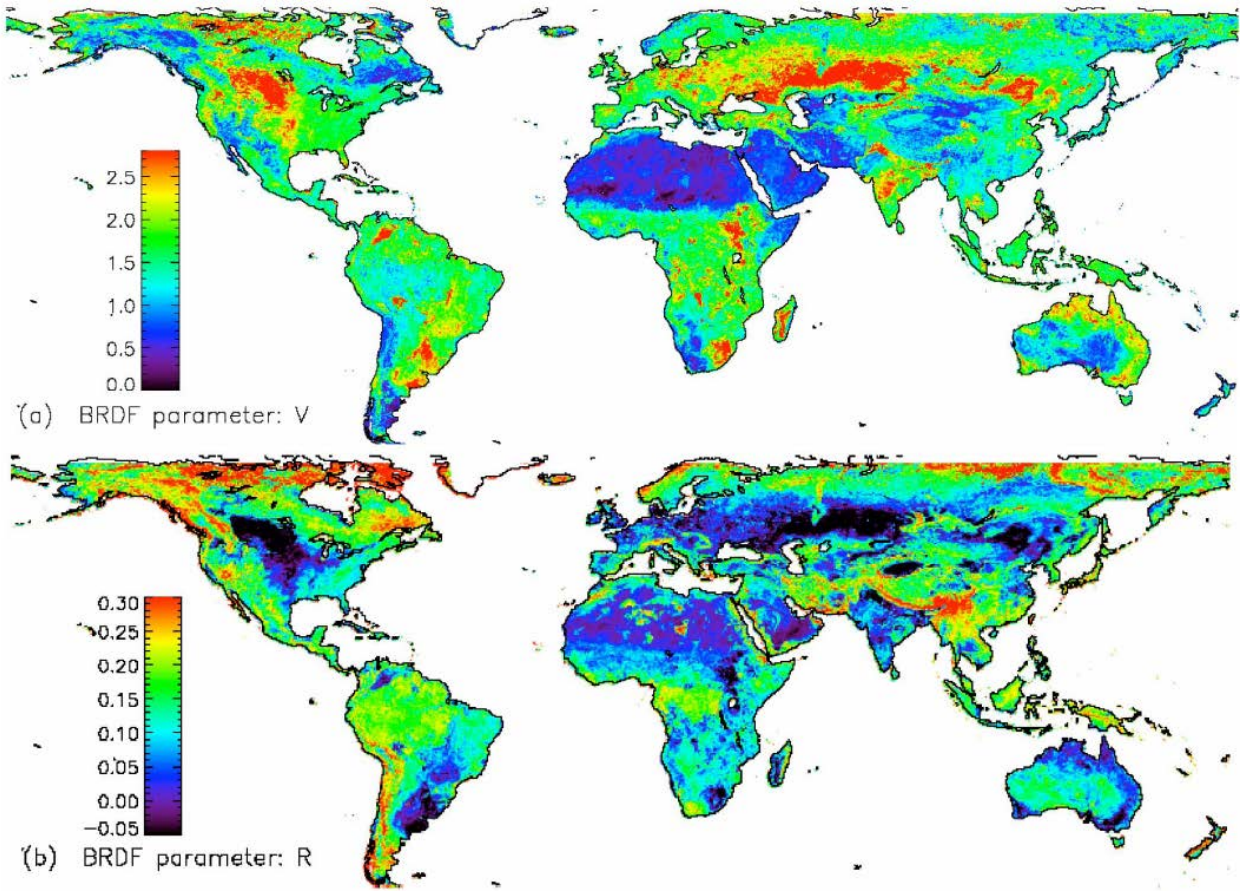


**Figure 10: Global map of the V (a) and R (b) parameters derived by Vermote et al. 2009 applied to the time series of Terra MODIS band 2 (2000–2004). V and R are shown for highest NDVI values of each pixel.**

### 3.4.1.6 Cloud, cloud-shadow masks

Cloudy pixels are detected based on difference with a MODIS monthly average Red band (MODIS Channel 1) BRDF corrected climatology. This climatology was computed on a per-pixel approach using 10 years of MODIS data. To compute a MODIS-like Red band, AVHRR data are spectrally adjusted using a 0.97 factor. Pixels are considered as cloud if the difference between the MODIS monthly average and the spectrally adjusted AVHRR is higher than 0.03.

Cloud height range (minimum and maximum) is estimated based on temperature derived from AVHRR Channel 4 and 5. Shadow pixels correspond to the projection of the Cloudy

pixels on the surface following the pixel location (lat, lon) – sun axe. Pixels detected as cloudy and shadow keep only the cloudy flag.

#### 3.4.1.7 NDVI Computation

NDVI is computed using the following equation:

$$NDVI = \frac{\rho_{830} - \rho_{640}}{\rho_{830} + \rho_{640}} \quad (37)$$

## 3.4.2 Data Merging Strategy

N/A

## 3.4.3 Numerical Strategy

N/A

## 3.4.4 Calculations

N/A

## 3.4.5 Look-Up Table Description

The quantities $\rho_o(\mu s,\mu v,\varphi)$ , $t_d(\mu)$ and S are functions of the optical thickness ($\tau$), single scattering albedo ($\omega$), and phase function ($P(\theta)$) of the scatterers and absorbers in the atmosphere. The calculation of $\rho_o(\mu s,\mu v,\varphi)$ , $t_d(\mu)$ and S is achieved with the aid of an atmospheric radiative transfer program such as the Dave and Gazdag (1970) model. However, it is computationally prohibitive to run a radiative transfer model for every pixel in a daily global data set. Thus, we created look-up tables with the 6S code (Vermote et al., 1997) which will supply the needed $\rho_o(\mu s,\mu v,\varphi)$, $t_d(\mu)$, and S for variety of sun-view geometries and aerosol loadings. $\rho_o(\mu_s,\mu_v,\varphi)$ are precomputed at 73 relative azimuth angles, 22 solar zenith angles, 22 view zenith angles and 10 aerosol optical depth. $t_d(\mu)$ is precomputed for 16 zenith angles and 10 aerosol optical thickness. S is precomputed for 10 aerosol optical thickness.

## 3.4.6 Parameterization

N/A

## 3.4.7 Algorithm Output

The outputs of the algorithm are 2 NetCDF files per day containing layers listed in Table 4 and Table 5. An example filename is:

AVHRR-Land_v004_AVH09C1_NOAA-16_20040812_c20130920200630.nc

With the following naming convention:

<***product-name***> = static series name of the product with the value, “AVHRR-Land”

<***product-version***> = product version number, “v004”

<***product-type***> = NASA product type identifier with the valid domain:
“AVH09C1” = AVHRR surface reflectance product
“AVH13C1” = AVHRR NDVI product

<***sat-id***> = Source NOAA satellite ID with the valid domain:
“NOAA-07”, “NOAA-09”, “NOAA-11”, “NOAA-14”, “NOAA-16”, “NOAA-17”, “NOAA-18”

<***YYYYmmdd***> = Date of the data in the file, formatted as year, month and day, with the valid range from “19810101” to present

c<***processing-date***> = Creation or processing date of the file identified with a ‘c’ followed by the year, month, day, hour, minute and second

.nc indicates the format (NetCDF)

**Table 4: Output layers AVH09C1**

| Name | Description | Units | Dimension |
|---|---|---|---|
| BT_CH3 | long_name = Brightness Temperature at 3.75 microns | degrees Kelvin | 3600X7200 |
| BT_CH4 | long_name = Brightness Temperature at 11.0 microns | degrees Kelvin | 3600X7200 |
| BT_CH5 | long_name = Brightness Temperature at 12.0 microns | degrees Kelvin | 3600X7200 |
| QA | long_name = Quality Control | | 3600X7200 |
| RELAZ | long_name = Relative Azimuth | degrees | 3600X7200 |
| VZEN | long_name = View Zenith Angle | degrees | 3600X7200 |
| SZEN | long_name = Solar Zenith Angle | degrees | 3600X7200 |
| TIMEOFDAY | long_name = Time since Start of Data Day | hours since 00:00:00 UTC | 3600X7200 |
| SREFL_CH1 | long_name = NOAA Climate Data Record of Surface Reflectance at 640 nm standard_name = surface_bidirectional_reflectance | - | 3600X7200 |
| SREFL_CH2 | long_name = NOAA Climate Data Record of Surface Reflectance at 830 nm standard_name = surface_bidirectional_reflectance | - | 3600X7200 |
| SREFL_CH3 | long_name = NOAA Climate Data Record of Surface Reflectance at 3.75 microns standard_name = surface_bidirectional_reflectance | - | 3600X7200 |
| longitude | long_name = longitude | degrees | 7200 |

| | | | |
|---|---|---|---|
| latitude | long_name = latitude | degrees | 3600 |
| lon_bnds | Top and bottom longitude of each grid cell | Degrees | 7200x2 |
| lat_bnds | Top and bottom latitude of each grid cell | Degrees | 3600x2 |
| time | long_name = time | days since 1981-01-01 00:00:00 UTC | 1 |

**Table 5: Output layers AVH13C1**

| Name | Description | Units | Dimension |
|---|---|---|---|
| NDVI | long_name = NOAA Climate Data Record of Normalized Difference Vegetation Index | - | 3600X7200 |
| QA | long_name = Quality Assurance | - | 3600X7200 |
| longitude | long_name = longitude | degrees | 7200 |
| latitude | long_name = latitude | degrees | 3600 |
| lon_bnds | Top and bottom longitude of each grid cell | Degrees | 7200x2 |
| lat_bnds | Top and bottom latitude of each grid cell | Degrees | 3600x2 |
| time | long_name = time | days since 1981-01-01 00:00:00 UTC | 1 |

# 4. Test Datasets and Outputs

## 4.1 Test Input Datasets

N/A

## 4.2 Test Output Analysis

### 4.2.1 Reproducibility

It is required to check the consistency of the calibration through time. As an example (Figure 11), the orbits of the AVHRR series onboard the 7, 9, 11 and 14 platforms were not stabilized. The overpass time drifts dramatically from the beginning of the lifetime to the end of each mission, introducing artificial variations due to increased atmospheric path length and surface directional effects (Privette et al., 1995).

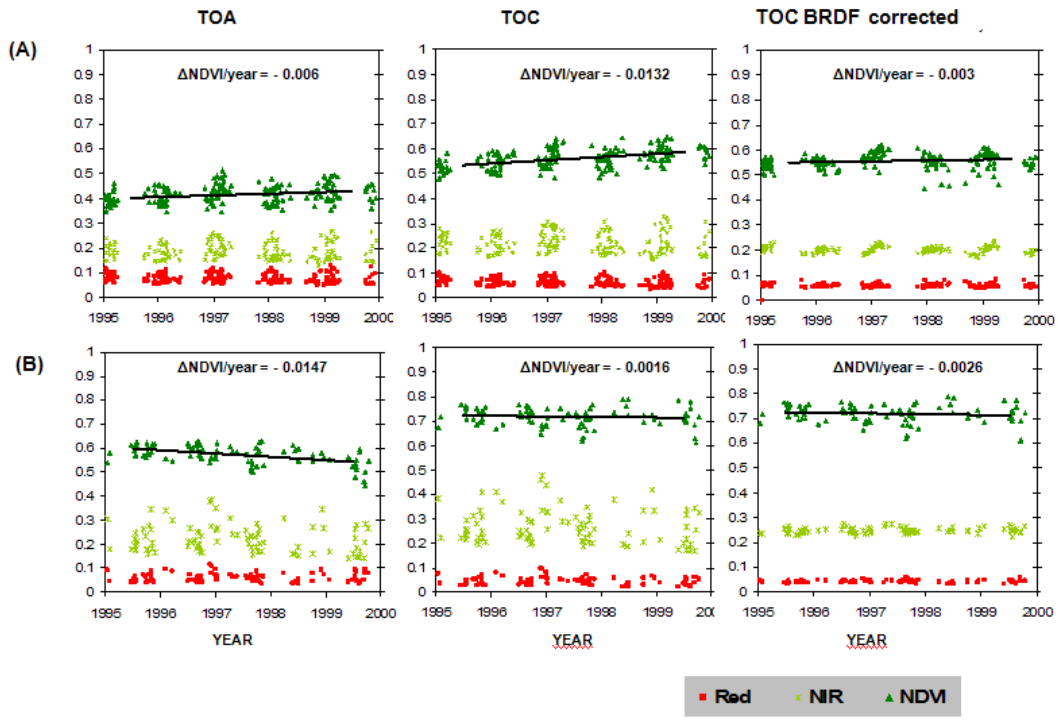


**Figure 11: Impact of the orbital drift on NOAA14 (1995-1999) data for two evergreen forest site in Australia, (A) with 50% tree cover, (B) with 95% tree cover. TOA is Top of the atmosphere; TOC is the Top of the canopy.**

Another example to check the reproducibility of sensor data is to cross-compare to other existing sensor data. In Figure 12, AVHRR nadir-corrected surface reflectance is compared to MODIS nadir-corrected surface reflectance acquired the same day. The RMSD is less than 0.03 for both spectral bands and 0.075 for NDVI. One source of deviation that is not taken into account is the spectral differences which can be identified using synthetic data. Figure 12-G shows the corrected NDVI after using a simple band-pass.

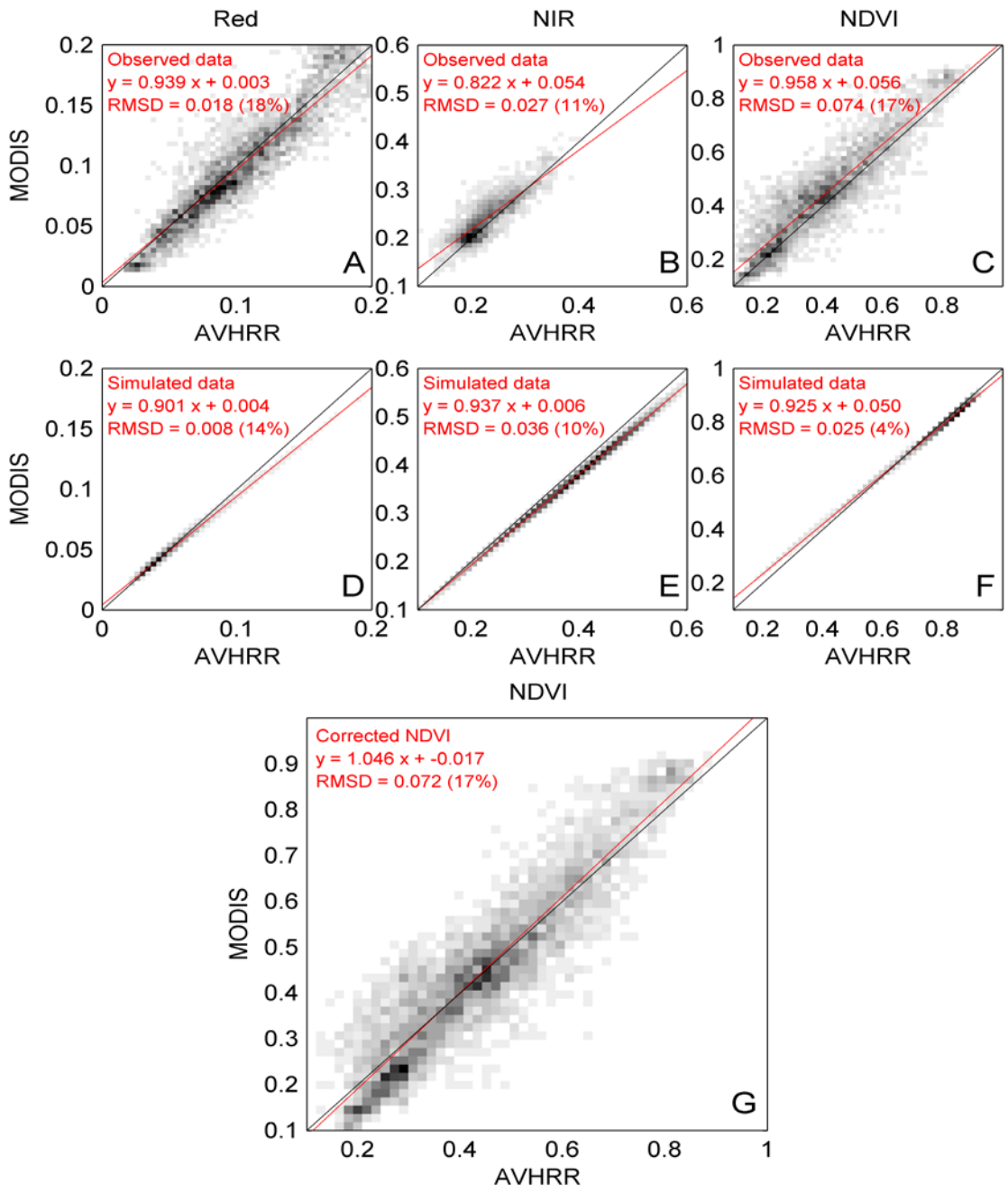


**Figure 12: Comparison of MODIS Aqua and NOAA16 AVHRR data, A (Red) ,B (NIR) ,C (NDVI) are observed over AERONET sites for 2003-2004 , D (Red), E (NIR), F (NDVI) are simulated using a vegetation model that account for spectral difference between MODIS and AVHRR bands. G shows over the AERONET sites MODIS NDVI versus corrected AVHRR NDVI computed from spectrally adjusted AVHRR surface reflectance.**

### 4.2.2 Precision and Accuracy

We have compared Version 2 Long Term Data Record (LTDR) data for 1999 with Pathfinder AVHRR Land (PAL) daily products (Saleous et al., 2000) over 48 sites distributed across the globe. Atmospheric data from AERONET (Holben, et al., 1998) sunphotometers at each site were used as input to the 6S radiative transfer model to atmospherically correct the top of the atmosphere AVHRR data to determine surface reflectance values for channels 1 and 2. Figure 13 shows that the LTDR data for channel 2 follow the one-to-one line very closely for surface reflectance values up to ~0.5. Similar LTDR results are obtained for channel 1, although the PAL data are closer to the 1-to-1 line. The LTDR data are clearly more accurate than the PAL values, and we anticipate obtaining agreement for higher surface reflectance values with an improved water vapor correction. For NDVI values we find the RMS error about the one-to-one line to be more than two times lower for the LTDR data than for the PAL values.

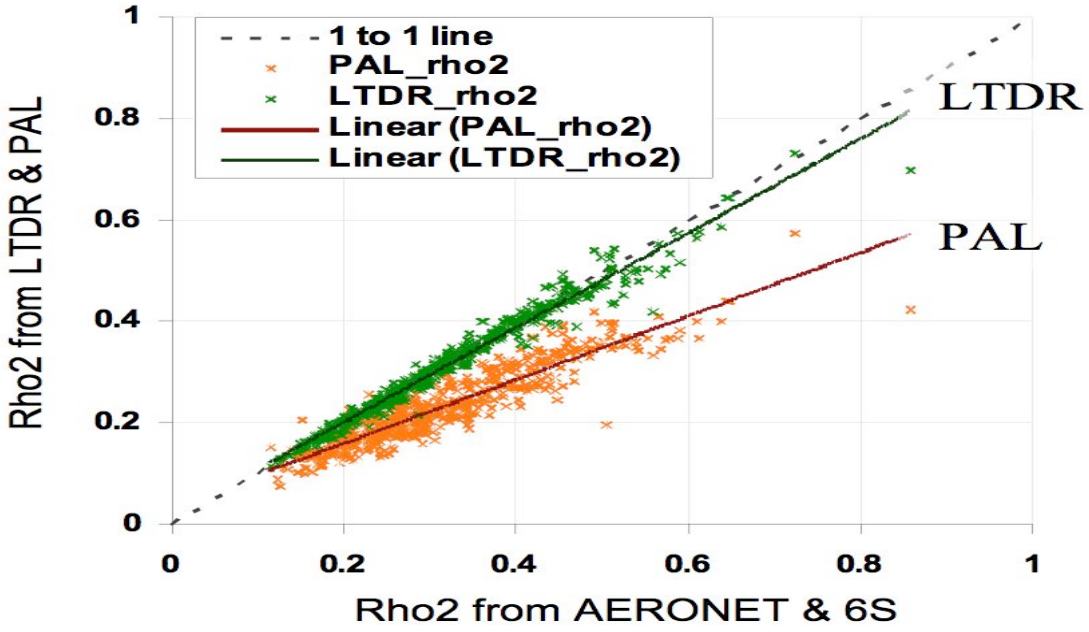


**Figure 13: Comparison of LTDR and PAL data for channel 2 at 48 AERONET sites for 1999 . The x-axis shows the surface reflectance values (rho2) determined from the 6S code supplied with atmospheric parameters from an AERONET sunphotometer, while the y-axis shows the surface reflectances retrieved from the AVHRR data using LTDR and PAL algorithms.**

Improper cloud and cloud shadow screening reduces the quality of the surface reflectance, may eliminate useful data and lead to misinterpretation of data time-series variability. Failure to remove sub-pixel and residual clouds may increase surface reflectance. Figure 14 shows the percentage of matching, false and missed cloud mask pixels over land between AVHRR and MODIS.

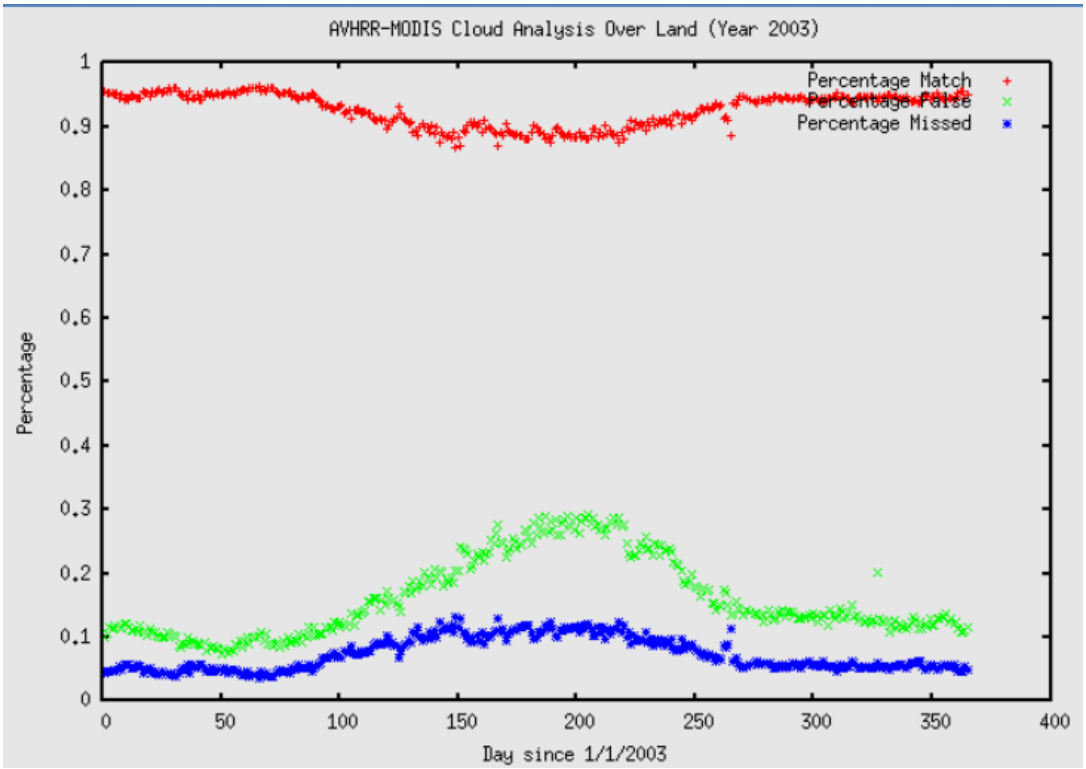


**Figure 14: Evaluation of the global performance of the LTDR v3 cloud mask Algorithm reported as percentage.**

### 4.2.3 Error Budget

Comparison of NDVI data from TOA, PAL and LTDR datasets with reference data at the AERONET stations are presented in Table 6. A, P and U metrics stand for Accuracy, Precision and Uncertainty, respectively. They are described in eq. 38-40 where ε and N correspond to the deviation between estimates and Aeronet reference and the number of points, respectively. The table showed that LTDR has better accuracy and precision when compared to PAL and TOA data. For the forest and savanna sites most of the data points (> 70%) had average atmospheric conditions (AOT = 0.05 to 0.25) and about 20% were hazy (AOT > 0.25). However, for semi-arid site more than half data points had clear atmospheric conditions (AOT < 0.05) and only 0.5% points were hazy. The direct validation shows that in hazy conditions all three datasets become very unreliable with precision as much as 0.22 in the forest site. These results show precision for TOA NDVI data between 0.023 for clear atmospheric conditions at the semi-arid site to 0.085 for average atmospheric conditions at the forest site (not considering data points with hazy atmospheric conditions). For LTDR NDVI data precision varied between 0.0061 for clear atmospheric conditions at semi-arid site to 0.0611 for average atmospheric conditions at forest site. A similar improvement in precision was observed at the savanna site.

$$A = \frac{1}{N} \times \sum_{i=1}^{N} \varepsilon_i \tag{38}$$

$$P = \sqrt{\frac{1}{N-1} \times \sum_{i=1}^{N} (\varepsilon_i - A)^2} \tag{39}$$

$$U = \sqrt{\frac{1}{N} \times \sum_{i=1}^{N} \varepsilon_i^{\,2}} \tag{40}$$

**Table 6: Accuracy (Eq. 38), precision (Eq. 39), and uncertainty (Eq. 40) for NDVI from simulated TOA and LTDR datasets. For the forest site; 20 (4%), 376 (75%), and 105 (21%) of 501 data points had clear, average, and hazy atmospheres respectively. For the savanna site; 40 (9%), 317 (71%), and 89 (20%) of 446 data points had clear, average, and hazy atmosphere respectively. For the semi-arid site; 384 (52%), 348 (47%), and 8 (1%) of 740 data points had clear, average, and hazy atmosphere respectively. A, P and U are statistical metrics (refers to Vermote and Kotchenova, 2008) standing for Accuracy, Precision and Uncertainty, respectively.**

| Simulated Data | Land cover | Clear (AOT < 0.05) | | | Average (AOT = 0.05 to 0.25) | | | Hazy (AOT > 0.25) | | |
|---|---|---|---|---|---|---|---|---|---|---|
| | | A | P | U | A | P | U | A | P | U |
| TOA | Semiarid | -0.062 | 0.023 | 0.066 | -0.067 | 0.023 | 0.071 | -0.140 | 0.063 | 0.151 |
| TOA | Savanna | -0.170 | 0.044 | 0.176 | -0.177 | 0.051 | 0.184 | -0.305 | 0.182 | 0.355 |
| TOA | Forest | -0.247 | 0.082 | 0.260 | -0.280 | 0.085 | 0.293 | -0.586 | 0.188 | 0.615 |
| PAL | Semiarid | -0.039 | 0.011 | 0.041 | -0.051 | 0.016 | 0.054 | -0.132 | 0.078 | 0.150 |
| PAL | Savanna | -0.079 | 0.015 | 0.081 | -0.107 | 0.043 | 0.115 | -0.252 | 0.171 | 0.305 |
| PAL | Forest | -0.056 | 0.026 | 0.061 | -0.124 | 0.072 | 0.143 | -0.508 | 0.219 | 0.553 |
| LTDR | Semiarid | -0.007 | 0.006 | 0.009 | -0.011 | 0.011 | 0.015 | -0.085 | 0.085 | 0.114 |
| LTDR | Savanna | -0.014 | 0.011 | 0.017 | -0.038 | 0.036 | 0.052 | -0.166 | 0.164 | 0.233 |
| LTDR | Forest | -0.025 | 0.021 | 0.032 | -0.085 | 0.061 | 0.104 | -0.429 | 0.199 | 0.473 |

# 5. Practical Considerations

## 5.1 Numerical Computation Considerations

No parallelization or difficulties in matrix inversions are expected. The algorithm implementation is based on LUTs to increase computation speed.

## 5.2 Programming and Procedural Considerations

N/A

## 5.3 Quality Assessment and Diagnostics

The estimate of the surface reflectance is accompanied with quality assurance information. QA bits contain information stored at the product resolution. Table 7 describes the bit ordering to use the Quality Control (AVH09C1) and Quality Assurance (AVH13C1) layers; notice that both use the same definitions.

**Table 7: AVH09C1 and AVH13C1 QA description. Bits are listed from the MSB (bit 15) to the LSB (bit 0).**

| Bit # | Description | Value=1 | Value=0 |
|---|---|---|---|
| 15 | polar flag (latitude over 60 degrees (land) or 50 degrees (ocean)); | yes | No |
| 14 | BRDF-correction issues; | yes | No |
| 13 | RHO3 value is invalid; | yes | No |
| 12 | Channel 5 value is invalid; | yes | No |
| 11 | Channel 4 value is invalid; | yes | No |
| 10 | Channel 3 value is invalid; | yes | No |
| 9 | Channel 2 value is invalid; | yes | No |
| 8 | Channel 1 value is invalid; | yes | No |
| 7 | Channels 1 - 5 are valid; | yes | No |
| 6 | Pixel is at night (high solar zenith); | yes | No |
| 5 | Pixel is over dense dark vegetation; | yes | No |
| 4 | Pixel is over sunglint; | yes | No |
| 3 | Pixel is over water; | yes | No |
| 2 | Pixel contains cloud shadow; | yes | No |
| 1 | Pixel is cloudy; | yes | No |
| 0 | (unused); | - | - |

## 5.4 Exception Handling

N/A

## 5.5 Algorithm Validation

The validation of the AVHRR surface reflectance was conducted over the AERONET data network as described in (Vermote and Kotchenova, 2008) as already introduced in section 4.1.3. Another validation process was the intercomparison with third

party sensor. After normalization for BDRF effects, the surface reflectance dataset was compared to moderate resolution sensor (e.g., MODIS, see section 4.1.1) to further provide an understanding of the performance of the product on a statistical basis (accuracy and precision).

## 5.6 Processing Environment and Resources

The CDR code is run on an 8-core 2.5GHz 64-bit Xeon server, running CentOS Linux 5.9 x86_64. The code was compiled with C-compiler GCC 4.4.7. The main C-libraries were: HDF5 8.88, HDF 4.2r4, NetCDF 4.2, Zlib 1.2, szip. A full year of AVH09C1 and AVH13C1 products is processed in 3.5 days corresponding approximately to a 100x speed.

# 6. Assumptions and Limitations

## 6.1 Algorithm Performance

This algorithm is constrained to land areas even if non-land areas are provided. Extreme angles, which may be encountered in polar regions, may cause large errors.

## 6.2 Sensor Performance

<Not Applicable>

# 7. Future Enhancements

## 7.1 Enhancement 1: Tropospheric Aerosol

Quality of the surface reflectance estimates is strongly driven by the knowledge of the aerosol optical thickness. Tropospheric Aerosol significantly impacts the signal. For example, Vermote et al. (2002) analyzed part of China (1600x1200km) for May 2000 and showed that even for a monthly composite, the aerosol effect still decreased the NDVI by 0.10 for 75% of the pixels due to tropospheric aerosols. Research efforts have shown the possibility of using the dark target technique on AVHRR (Saleous et al., 2000) based on the middle-infrared reflectance (Roger and Vermote, 1998) to account for tropospheric aerosols.

## 7.2 Enhancement 2: Water Vapor

For AVHRR, over barely vegetated surfaces, atmospheric water vapor can introduce variations up to 0.11 in the NDVI. That is relatively very important given the low NDVI signal for those areas (typically 0.1 to 0.2) (Tanre et al., 1992). Ancillary data sources for water vapor (National Center of Environmental Prediction - NCEP) were evaluated and the corrections for the water vapor effect in AVHRR were implemented in the LTDR code. We will further evaluate the water vapor correction and try to improve the correction by deriving water vapor directly from the AVHRR data using the longwave split window technique. The coefficient for the split window technique will be derived by comparing NOAA 16 AVHRR with near coincident water vapor retrievals from MODIS Aqua (using the near infrared differential absorption technique, Vermote and Saleous, 2006) as illustrated in Figure 15.

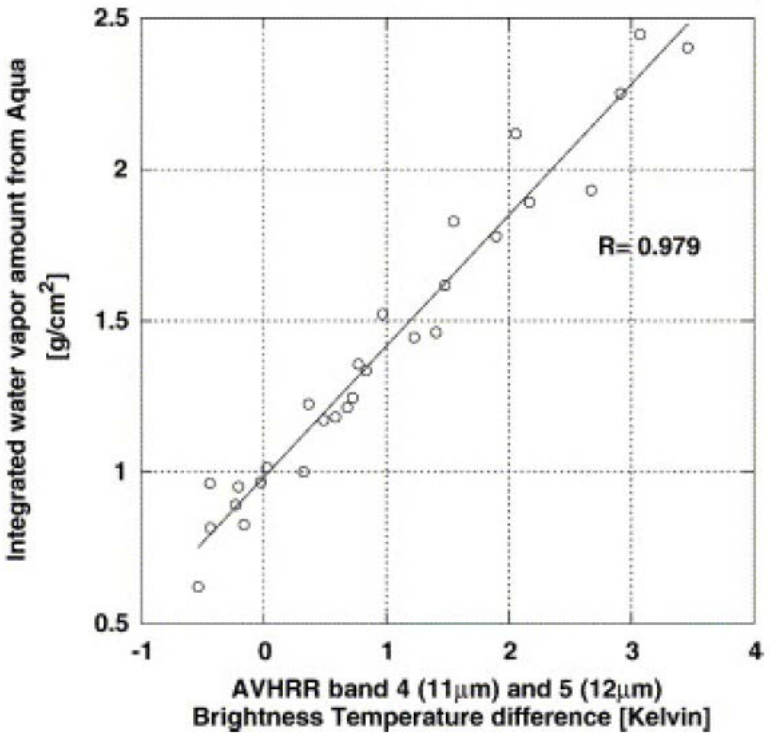


**Figure 15: Integrated water vapor content derived from Aqua MODIS near-infrared absorption bands (18 and 19) as a function of the temperature difference in bands 4 (11 µm) and 5 (12 µm) for AVHRR NOAA16 data collected over a desert site.**

# 8. References

Breon, F. M. F. Maignan, M. Leroy, and I. Grant (2002). "Analysis of hot spot directional signatures measured from space" J. Geophys. Res., vol. 107, no. D16, p. 4282.

Dave, J. V. and J. Gazdag, (1970). A modified Fourier transform method for multiple scattering calculations in a plane parallel Mie atmosphere. *Applied Optics*,9,1457-1466.

Fraser, R. S. *et al*., (1989). Algorithm for atmospheric corrections of aircraft and satellite imagery. *NASA Technical Memorandum* 100751,98 pp.

Fraser, R. S. R. A. Ferrare, Y. J. Kaufman and S. Mattoo (1992). Algorithm for atmospheric corrections of aircraft and satellite imagery. Int. J. Remote Sensing, 13, 541-557.

Gao, B.C. and Y.J. Kaufman, (1993). Water vapor retrieval from MODIS.

Holben, B. N. *et al*. (1998). AERONET - A federated instrument network and data archive for aerosol characterization. *Remote Sensing of Environment*, 66(1), 1-16.

Kaufman Y. J. and D. Tanr(1998). Algorithm for remote sensing of aerosol from MODIS. MODIS Algorithm Theoretical Basis Document.

King M., Harshvardhan D. and A. Arking (1984). A model of the radiative properties of the El Chichon stratospheric aerosol layer. J. Clim. Appl. Meteorol.,23,1121-1137.

Lenoble, J., (1993). Atmospheric Radiative Transfer. *Hampton*, VA. A. Deepak Publishers, 532 pp.

McClatchey, R. A., *et al*. (1971). Optical properties of the atmosphere. AFCRL-71-0279, *Air Force Cambridge Research Lab*, Hanscom AFB MA.

McCormick, M.P. and R. E. Viega, (1992). Sage II Measurements of early Pinatubo Aerosols. ,19,155-158.

NOAA, (1988). Data Announcement 88-MGG-02, Digital relief of the Surface of the Earth. National Geophysical Data Center, Boulder, Colorado,.

Privette, J. L., *et al*. (1995). Effects of orbital drift on advanced very high resolution radiometer products: Normalized difference vegetation index and sea surface temperature. *Remote Sensing of Environment*, 53(3), 164–171

Roger, J. C., and Vermote, E. F., (1998). A method to retrieve the reflectivity signature at 3.75mm from AVHRR data. Remote Sensing of Environment, 64, 103–114

Saleous El, NZ, Vermote, EF, Justice, CO, Townshend, JRG, Tucker, CJ, Goward, SN (2000). Improvements in the global biospheric record from the Advanced Very High Resolution Radiometer (AVHRR). INTERNATIONAL JOURNAL OF REMOTE SENSING, 21(7-Jun), 1251-1277.

Tanré, D. *et al*., (1990). Description of a computer code to simulate the satellite signal in the solar spectrum: 5S code*. Int. J. Remote Sensing*,11,659-668.

Tanr, D., Holben, B. N. and Kaufman, Y. J. (1992). Atmospheric Correction algorithm for NOAA-AVHRR Products: Theory and Application. IEEE Transaction on Geoscience and Remote Sensing, 30, 231-248.

Vermote, E. F. *et al*. (1994). Stratospheric aerosol perturbing effect on the remote sensing of vegetation: Correction method for the composite NDVI after the Pinatubo eruption*. ISPRS symposium on Physical measurements and signature in remote sensing*, Val d'Isére, France, January 1994 .

Vermote, E. F. *et al*. (1997). Second Simulation of the Satellite Signal in the Solar Spectrum: an overview, *IEEE Transactions on Geoscience and Remote Sensing*, 35,3.

Vermote, E. F. *et al*. (2002). Atmospheric correction of MODIS data in the visible to middle infrared: first results, *Remote Sens. Environ*., 83, 97-111.

Vermote E.F., N.Z. Saleous (2006). Calibration of NOAA16 AVHRR over a desert site using MODIS data. Remote Sensing of Environment, Volume 105, Issue 3, Pages 214-220, ISSN 0034-4257.

Vermote, E.F., & Kotchenova, S. (2008). Atmospheric correction for the monitoring of land surfaces. *Journal of Geophysical Research-Atmospheres, 113*, D23S90.

Vermote, E., *et al*. (2009). Towards a Generalized Approach for Correction of the BRDF Effect in MODIS Directional Reflectances. *Ieee Transactions on Geoscience and Remote Sensing*, 47, 898-908.

# Appendix A. Acronyms and Abbreviations

| Acronym or Abbreviation | Meaning |
|---|---|
| 6S | Second Simulation of a Satellite Signal in the Solar Spectrum |
| AERONET | AErosol RObotic NETwork |
| AOT | Aerosol Optical Thickness |
| AVHRR | Advanced Very High Resolution Radiometer |
| BRDF | Bidirectional reflectance distribution function |
| C-ATBD | Climate Algorithm Theoretical Basis Document |
| CDR | Climate Data Record |
| DEM | Digital elevation model |
| GAC | Global Area Coverage |
| LSB | Least significant bit |
| LTDR | Long Term Data Record |
| MODIS | Moderate Resolution Imaging Spectroradiometer |
| MSB | Most Significant Bit |
| NCDC | National Climatic Data Center |
| NCEP | National Centers for Environmental Prediction |
| NDVI | Normalized Difference Vegetation Index |
| NIR | Near infrared |
| NOAA | National Oceanic and Atmospheric Administration |
| PAL | Pathfinder Land |
| QA | quality assurance |
| QC | quality control |

| Acronym or Abbreviation | Meaning |
|---|---|
| SR | Surface Reflectance |
| TOA | top of atmosphere |
| TOC | top of canopy |